



A novel electric-assisted photocatalytic technique using self-doped TiO₂ nanotube films

Honghui Pan^{a,1}, Minghui Sun^{a,1}, Xiaoguang Wang^a, Ming Zhang^b, Muthu Murugananthan^c, Yanrong Zhang^{a,*}

^a School of Environmental Science and Engineering, Huazhong University of Science and Technology, Wuhan 430074, PR China

^b Geological Survey of Japan, National Institute of Advanced Industrial Science and Technology, Tsukuba, Ibaraki 305-8567, Japan

^c Department of Chemistry, PSG College of Technology, Peelamedu, Coimbatore 641004, India

ARTICLE INFO

Keywords:

Electric-assisted photocatalysis
Self-doped TiO₂ nanotube film
Carrier separation
Water splitting
H₂O₂ synthesis
CO₂ photoreduction

ABSTRACT

Semiconductor doping is an effective strategy for improving the light absorption efficiency and the photo-generated carrier transport in photocatalysts. However, bulk defects induced by doping act as recombination centers, accelerating the recombination of carriers, which is detrimental to the photocatalytic performance. In this study, a novel electric-assisted photocatalytic technique was developed to reduce the recombination of the carriers trapped by the defects. The technique involves applying a low external voltage to a self-doped TiO₂ nanotube film, without any electrolyte and counter electrode. The remarkable improvement in the charge carrier dynamics under the electric assistance is attributed to the significant promotion of photogenerated electron fluxes and prevention of charge recombination. The electric-assisted photocatalytic technique is compatible with a liquid- or a gas-phase reactive system, e.g., water splitting, H₂O₂ synthesis, and CO₂ photoreduction. The technique is sufficiently advanced to allow scale-up of the photocatalytic process from laboratory scale to industrial-scale.

1. Introduction

Heterogeneous semiconductor photocatalysis is a promising strategy for the sustainable use of solar energy to address both environmental issues and the energy crisis. To date, different types of photocatalysts have been developed, such as metal oxide-based [1,2], graphitic carbon nitride (g-C₃N₄)-based [3,4], metal-organic frameworks (MOFs) [5,6], and covalent-organic frameworks (COFs) [7,8] photocatalysts, which provide a technical basis for both academic research and engineering applications of photocatalysis. Among the many types of photocatalysts available, TiO₂-based photocatalysts have a long history and are most commonly used because TiO₂ has an excellent photocatalytic performance, high stability and low cost. In addition, it is known to be safe for both the environment and humans. TiO₂-based photocatalysts have a unique set of physicochemical properties that allow light irradiation to generate highly reactive intermediates for the degradation of pollutants and the synthesis of value-added chemicals, e.g., H₂ production via the water-splitting reaction (WSR), H₂O₂ production via the oxygen

reduction reaction (ORR), and formation of non-fossil fuels via CO₂ photoreduction (CO₂-PR). However, these processes still suffer from some disadvantages such as low light harvesting efficiency, spatial charge separation, and surface reactivity. Mechanistic studies revealed that the dominant factor affecting the overall efficiency of the photocatalytic processes is the existence of defects in the photocatalytic materials. Therefore, much effort has been devoted to defect engineering in the photocatalytic materials in order to improve the photocatalytic efficiency [9,10]. In the case of TiO₂ semiconductors, oxygen vacancies (OVs, self-doping) can be created by removing the lattice oxygen atoms through the defect engineering [11]. This self-doping treatment can increase the conductivity of the semiconductor even comparable to that of a semi-metal [12], thereby reducing the resistance barrier for charge transport and increasing the photocatalytic performance.

The photocatalytic process is complicated and includes multiple tandem steps, in which the faster recombination of photogenerated electron-hole pairs compared to their interfacial transfer is fatal to the efficiency. Because the defects provide the majority of the electron-hole

* Corresponding author.

E-mail address: yanrong.zhang@hust.edu.cn (Y. Zhang).

¹ These authors contributed equally to this work. All authors have given approval to the final version of the manuscript.

recombination sites, their introduction, especially those being introduced into the semiconductor bulk, is inevitably detrimental to the photocatalytic performance of the semiconductor [13,14]. Therefore, it is important to overcome the electrostatic force to achieve spatial separation of the electron-hole pairs in the bulk defects. A strategy for the partial reduction of the electrostatic force is to create an electric field within photocatalyst, forcing the photogenerated carriers to move in opposite directions, increasing the charge transfer rate of the carriers and decreasing their recombination rate. Photoelectrocatalysis (PEC) is a technique, in which an external potential bias is applied to a semiconductor (photoelectrode) and the charge carriers are driven out of the illuminated semiconductor film to a counter electrode (CE). However, the PEC system is conventionally applied in the liquid phase [15–17]. The complex structure of the separated electrode (CE), introduced electrolyte solution, and undesirable consumption of electric energy in the solution limit the practical applications of this technique [18,19]. In particular, this technique is not suitable for gas-phase processes, which are very important and constitute a broad area of photocatalytic applications such as CO₂ photoreduction [20–23].

In this study, a novel electric-assisted photocatalytic system, without any electrolyte and counter electrode, was developed with a solo film of self-doped TiO₂ nanotube (R-TNTs). Upon the application of an external voltage to films with different cocatalysts such as Pt, Pd and Au, the efficiency of the liquid-solid or the gas-solid heterogeneous photocatalytic WSR, ORR and CO₂-PR reactions increased dramatically. Based on the construction of the electric-assisted photocatalytic systems, we report the combination of transient photocurrent techniques and photoelectric characterization with operando steady-state photoluminescence (PL) as well as time-resolved photoluminescence (TRPL) to determine different aspects of the photoelectric-induced charge dynamics in the reaction systems. The present study revealed that the external voltage was especially allowed for efficient spatial separation of the charge carriers and quenching of the recombination caused by the defects, thus greatly improving the photocatalytic activity of the self-doped catalysts. The high conductivity obtained by the self-doping process is beneficial for the transport of photogenerated carriers, while the synchronous introduction of OV defects is probably detrimental to the photocatalytic efficiency. The electric assistance resolved this contradiction, thereby promoting electron transfer kinetics within the photocatalytic systems. Elucidation of the impacts of external voltage on kinetics and mechanisms of charge transfer in semiconductors is of great significance. The findings obtained from the present study would afford new opportunities and possibilities for the construction of efficient photocatalytic systems with other doped catalysts and promote their wider application.

2. Experimental

Refer to the [Supporting information](#) for the materials, the fabrication of catalysts, and the general characterization.

2.1. Electric-assisted photocatalytic test

The size of each catalyst was 5 cm × 1 cm × 8 μm (for WSR and ORR) and 2 cm × 1 cm × 8 μm (for CO₂-PR), prepared on a 0.1-mm-thick Ti substrate with Ti exposed on both ends (the photocatalyst used in this study is of this specification unless noted otherwise). For the WSR (Fig. S1a) and ORR (Fig. S1b) systems, a catalyst film bended in U-shape was partially immersed in 5 ml deionized water in a 20 ml sealed quartz reactor, and the two ends exposed in the gas were connected to a DC voltage with Cu wires. Since the electrical resistivity of deionized water (18.25 MΩ cm⁻¹) is much greater than that of the catalyst film, no short circuit occurred in the electrical system. The reactor for the WSR and ORR systems was filled with Ar and O₂ gas, respectively. In the CO₂-PR system, Cu wires were connected to both ends of the rectangular catalyst film (Fig. S1c). Before each test run, the reactor was purged with

ultrapure CO₂ gas at a flow rate of 50 ml min⁻¹ for 30 min through a gas-washing bottle containing an aqueous solution, to fill with a CO₂/H₂O gas mixture (water vapor concentration ≈ 2.5% by volume, RH = 80%, 298 K, 1 atm). A single-wavelength-shallow UV LED lamp (365 nm) was used as the light source. The distance between the photocatalyst and the LED lamp was kept at 5 cm during the experiments. The effective mass of the catalyst film was approximately 10 mg. A steady-state direct current (DC) power source was used for the voltage supply in the photocatalytic tests. During the test runs, the reactor was cooled to approximately 298–303 K through water circulation.

The concentration of H₂O₂ was determined by both the potassium permanganate titration and the potassium titanium oxalate spectrophotometric methods for mutual authentication [24]. The gaseous products, such as H₂, O₂, and hydrocarbons, were quantified using a gas chromatography (GC, 7820 A, Agilent Technologies). For the isotopic test of CO₂-PR, the products were detected using a gas chromatography-mass spectrometry (GC-MS, 7890 B, Agilent Technologies). The detailed parameters are provided in the [Supporting information](#).

2.2. Conductivity, carrier concentration and the measurement of I-V curve

Free-standing membrane catalysts were prepared for the conductivity measurements. The as-prepared TiO₂ nanotube arrays (TNTs) and R-TNT catalysts were sonicated in deionized water for 10 min and dried to obtain a clean surface, and then peeled off carefully from the Ti substrate with a tape to obtain the free-standing membranes (Fig. 1a).

The two tips connected to the working and the counter electrodes (together with the reference electrode) of an electrochemical station (CHI760E, USA) were wrapped with Ti foil and used for conductivity measurements. The two Ti foil wrapped tips were touched on the surface of the catalyst, by which ohmic contact was formed between the Ti foil and the TiO₂ based catalysts. The electrochemical station was operated under the steady state DC mode, and the currents (*I*) under different potentials (*V*) were obtained. The length (*L*) and the cross-sectional area (*S*) of the catalyst between the two tips was measured to determine the conductivity of the catalyst. The final result was the average of multiple measurements of *I*-*V* with different *L* and *S* values. The carrier concentrations of the materials were measured using a Hall effect meter (ECOPIA HMS-5500, Korea).

The measurement of the *I*-*V* curves for the free-standing catalysts was carried out using the electrochemical station by applying the DC voltages between 0.01 and 1.5 V. The catalyst was fixed on an insulating glass slide, kept 1 cm apart from the LED light source, with a 2 cm² area under illumination. The catalyst was electrically connected via two pieces of Ti foil during the measurement, as shown in Fig. 1a.

2.3. Operando characterization

The operando steady-state PL (LabRAM HR800, Horiba JobinYvon) was carried out using a fluorescence spectrometer with an excitation source wavelength of 325 nm (Fig. S2). Time-resolved PL (Horiba Scientific, DeltaPro) decay spectra were obtained by excitation of the photocatalysts at 350 nm (Fig. S3), that is, within the TiO₂ band gap, and the detection wavelengths were 500 and 550 nm, respectively. Before each measurement, the photocatalyst, with Cu wires connected at both ends of the exposed Ti substrate, was placed in a 20 ml sealed quartz vessel which was then fed with Ar or CO₂ gas. The exposed Ti and Cu were covered with insulative epoxide. A steady-state DC power source was used for the voltage supply.

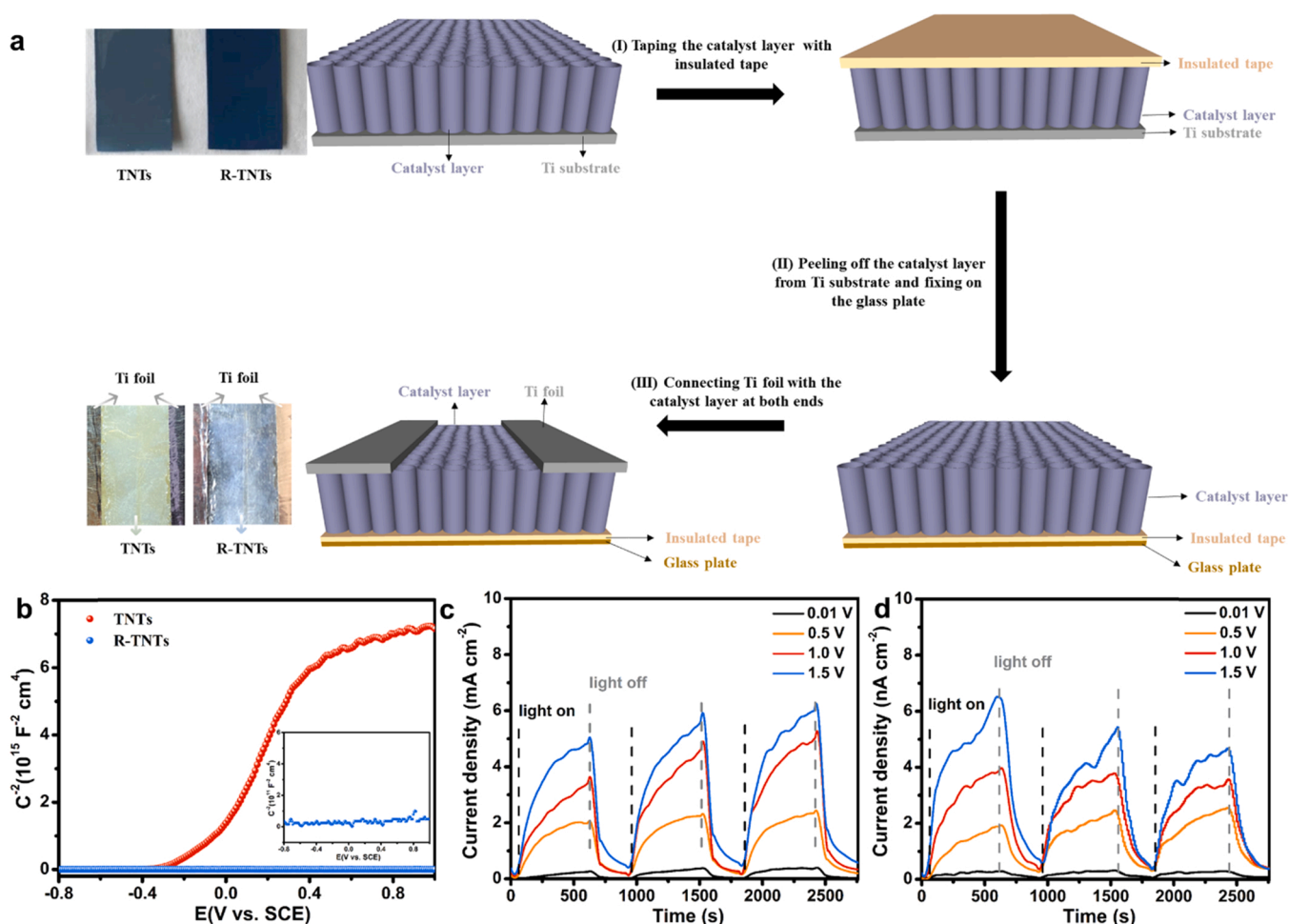


Fig. 1. (a) The mechanical peeling and component integration of the TNTs and the R-TNTs. (b) The Mott-Schottky curve. The I - V curves of (c) the R-TNTs and (d) the TNTs free-standing films with different voltages under light irradiation. Note the difference between the units used for current density in (c) and (d).

3. Results and discussion

3.1. Photoelectric current analysis and electric properties of the self-doped TNTs

Field emission scanning electron microscopy (FE-SEM) showed the morphology of the TiO_2 nanotube arrays (inner diameter: 150 nm, outer diameter: 180 nm, length: 8 μm , as depicted in Fig. S4) on the Ti substrate. The anatase lattice orientation (Fig. S5) in the TiO_2 catalysts was determined using X-ray diffraction (XRD). In the X-ray photoelectron spectroscopy (XPS) of Ti 2p (Fig. S6), a negative shift of 0.42 eV in the binding energy (BE) was observed for the R-TNTs compared to that of the TNTs. In contrast, the characteristic peak in the high resolution O 1s XPS spectra exhibited a positive shift of 0.35 eV (Fig. S7). Moreover, the deconvoluted peaks of 531.2 and 529.9 eV from the O 1s were ascribed to adsorbed -OH and O-Ti-O species on the surface of TNTs. Upon the self-doping treatment, a new deconvoluted peak formed at 530.4 eV was attributed to the presence of O-Ti-Ov. By applying further constraints on the characteristic peak positions for Ti^{3+} (531.2 and 529.9 eV), Ti^{4+} (531.2 and 529.9 eV), adsorbed -OH, O-Ti-Ov and O-Ti-O, the relative amounts of surface composition could be roughly determined from the peak area ratio [25,26]. As seen in Table S1, the relative ratio of Ti^{3+} in TNTs was found to increase from 18.5% to 67.5% upon self-doping. Furthermore, the increase was also observed from the both O-Ti-Ov (from 0% to 39.9%) and adsorbed -OH (from 26.5% to 31.9%) species, along with the decrease from the O-Ti-O (from 73.3% to 28.2%) (Table S2), confirming the existence of OV in the R-TNTs. According to

the results obtained from the Ti 3p and O 1s XPS spectroscopy analyses, the surface atomic composition of TNTs and R-TNTs was determined to be $\text{TiO}_{1.90}\text{H}_{0.50}$ and $\text{TiO}_{1.67}\text{H}_{0.53}$, respectively.

A combination of the electronic properties and the photoelectric current analysis can provide a complete scheme of the transport of the charge carriers confined within the catalysts. This information is essential for understanding the voltage-driven processes under light irradiation in photocatalytic reactions. To realize this objective, the carrier concentration (n) and the conductivity (σ) of the catalysts were measured using the Hall effect and the two-probe method [12,27], respectively. As shown in Table S3, the self-doping treatment of the TNTs changed its electronic structure greatly, increasing the n of the TNT films from $1.82 \times 10^{15} \text{ cm}^{-3}$ to $1.21 \times 10^{20} \text{ cm}^{-3}$, which was consistent with their magnitudes from the Mott-Schottky plot measurements (Fig. 1b, $2.36 \times 10^{15} \text{ cm}^{-3}$ for the TNTs and $4.73 \times 10^{20} \text{ cm}^{-3}$ for the R-TNTs) [28]. Due to the high carrier density (up to 10^{20} cm^{-3}), the R-TNTs has changed to be a semimetal, unlike the TNTs remained to be an n-type semiconductor. When the typical n-type semiconductor is in contact with an electrolyte, the thickness of the space charge layer becomes much larger than the Helmholtz layer, and the bias voltage mainly applies on the space charge layer. Therefore, the Mott-Schottky curves of the TNTs show a voltage-dependent capacitance as described by Eq. S1 [12]. While in the case of the R-TNTs, the capacitance of the Helmholtz layer (C_H) at the solid-liquid interface becomes comparable to the space charge capacitance (C_{sc}) of the R-TNTs, and the influence of bias voltage on C_H cannot be neglected. The modified Mott-Schottky equation (Eq. S2) considering the effects of bias voltage on C_H behaves

differently from the Eq. S1 [29]. In addition, upon the self-doping, the carrier populations increased dramatically from 113 to 7.5×10^6 per tube in the bulk of the photocatalyst (the detailed calculation is depicted in Supporting information). The enhanced carrier concentration promoted the conductivity of the photocatalyst from $4.54 \times 10^{-8} \text{ S cm}^{-1}$ for the TNTs to $4.22 \times 10^{-2} \text{ S cm}^{-1}$ for the R-TNTs. The effective electron mobility (μ) can be calculated using the following expression [30]:

$$\sigma = ne\mu \quad (1)$$

Where e denotes the elementary charge. An approximately 14-fold increase in mobility was achieved by the self-doping treatment. Furthermore, the electrochemical impedance spectroscopy (EIS) of the R-TNTs (Fig. S8) showed a representative Nyquist plot with a smaller arc radius than that of the TNTs. The correspondingly lower electron-transfer resistance facilitated an effective charge transfer to the reaction interface within the catalyst.

I - V curves were measured using free-standing catalysts to investigate the effect of external voltages on the photogenerated carriers (Fig. 1a). The photocurrent increased with the increase in external voltage applied on the catalyst film from 0 to 1.5 V under light irradiation. For the R-TNTs, the photocurrent dramatically increased to 5.02 mA cm^{-2} from a dark current of 0.18 mA cm^{-2} (Fig. 1c) under the voltage of 1.0 V. While for the TNTs, it increased only from 0.30 to 4.06 nA cm^{-2} (Fig. 1d). The net photocurrents recorded represent electron fluxes in response to the applied voltage under light irradiation. The photoelectron flux generated in the R-TNTs was far greater than that generated in the TNTs under the same voltage. Because the photocurrent is proportional to the concentration and the mobility of carriers, it is not surprising that a larger photocurrent of six orders of magnitude was observed from the R-TNTs compared to that from the TNTs under the same electric field gradient.

Photoredox occurs on the photoelectrode and the CE separately in the conventional PEC. However, in the electric-assisted photocatalytic system, they are integrated into a single piece of catalyst film, which has

been confirmed from the photoelectric reduction of H_2PtCl_6 and oxidation of $\text{Pb}(\text{NO}_3)_2$ [31]. When a 5 ml aqueous droplet containing 1 mM H_2PtCl_6 and 2 mM $\text{Pb}(\text{NO}_3)_2$ was spread over one side of the R-TNT film, and then subjected to 1.0 V under light irradiation for 1 h, Pt and PbO_2 were found to be co-dispersed on the catalytic film (Fig. S9–S11). Compared to photocatalytic deposition, photoelectric-deposition achieved over 18.5 times Pt at% and 6 times Pb at% (Fig. S12), respectively. It is worth noting that no Pt and PbO_2 were deposited on the R-TNT film without light irradiation even under an external voltage of 1.5 V.

3.2. Electric assisted carrier separation

Operando steady-state PL and TRPL spectroscopies were measured to clarify the effects of the external voltage on the carrier dynamics. The PL spectra obtained from the R-TNTs and TNTs with different voltages, which were measured in Ar or ambient atmosphere at room-temperature, are presented in Fig. 2a. These spectra showed broad visible photoluminescent signals in the range of 400–800 nm, associated with several radiative and/or non-radiative luminescent centers generated from the defect [32]. The characteristic PL peak of R-TNTs showed a blue-shift from 560 to 515 nm, compared to that of the TNTs. In the Ar atmosphere, full recombination of the photogenerated carriers in the respective catalysts led to the most intense PL signals. However, the R-TNTs exhibited a stronger inhibition against the carrier recombination owing to its high conductivity, for which its PL intensity was two-third that of the TNTs. Upon switching to the ambient atmosphere, the catalysts exhibited rapid quenching of the PL signals. When the R-TNTs were applied with higher voltages, the intensity of peaks continuously declined along with a red-shift of peak center from 515 to 530 nm. Moreover, the intensity ratio of the R-TNTs to TNTs significantly decreased from about two-third to one-third as the external voltage elevated from 0 to 1.5 V.

The PL spectra of both types of catalysts in the ambient atmosphere

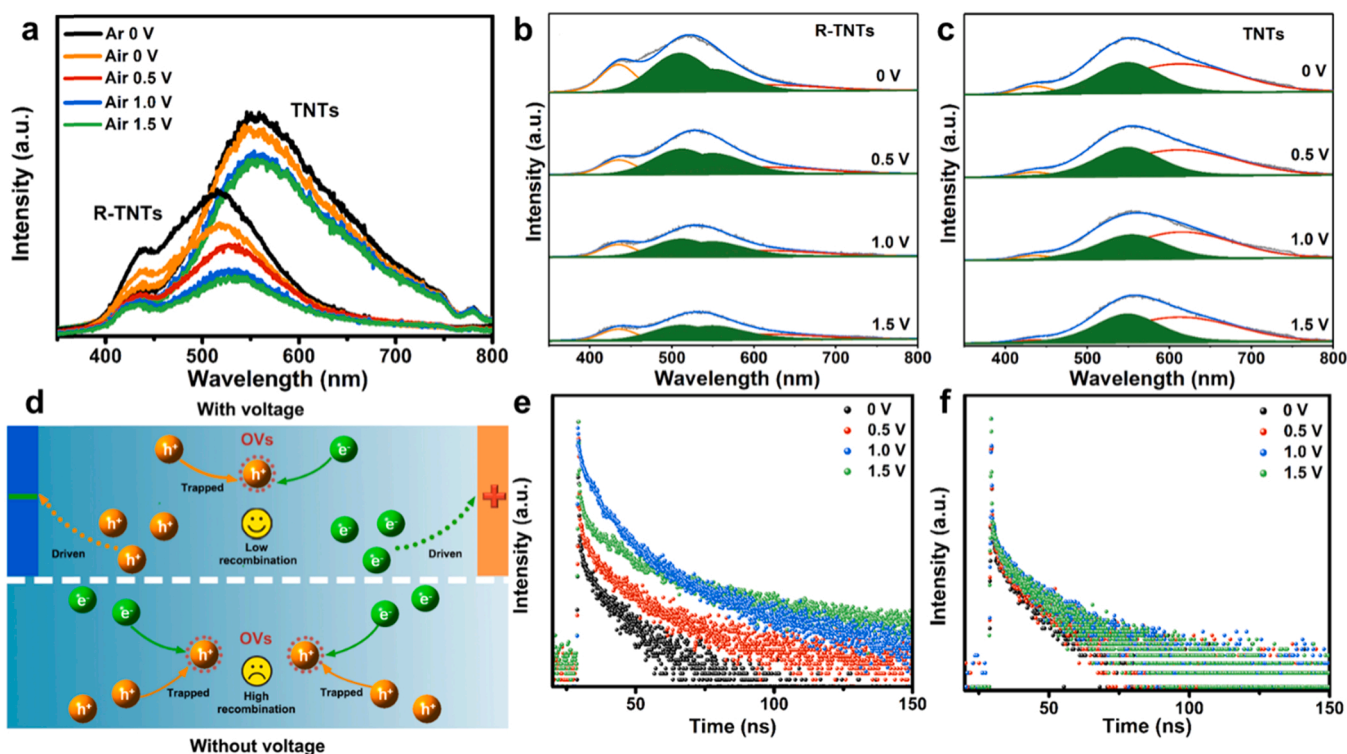


Fig. 2. (a) Operando-PL spectra of the R-TNTs and TNTs, and (b-c) their deconvoluted spectra under ambient atmosphere, with the different external voltages. (d) Schematic of photogenerated carrier migration and recombination with or without external voltage. Operando time-resolved fluorescence emission decay spectra of (e) the R-TNTs and (f) the TNTs with the different bias voltages in ambient atmosphere. The detection wavelength was 550 nm.

can be deconvoluted into four peaks (Fig. 2b and c), which are centered at 435 nm (A, orange), 510 and 550 nm (B, green), and 610 nm (C, red). The orange component at 435 nm was ascribed to recombination of self-trapped excitons, the two green peaks at 510 and 550 nm were attributed to the recombination of mobile electrons with trapped holes (bulk defects, such as bulk OV), while the red component at 610 nm was assigned to the recombination of trapped electrons (surface states, such as surface $\text{Ti}^{4+/3+}$) with mobile holes [33–35]. The R-TNTs features predominantly the green PL signals, which are related to the formation of larger amounts of OVs [36]. Furthermore, the external voltage evidently quenched the PL signal of the R-TNTs, in which the combination ratio of the mobile electrons to OVs (B/C) was damped from 5.0 to 2.9, compared to that of the TNTs, where there was an insignificant change (0.8) in this ratio (Fig. 2(b and c) and Table S4). Under the illumination, the photogenerated holes were trapped by bulk OVs introduced by self-doping, and therefore attracted mobile electrons via the electrostatic force, resulting in a high recombination. In contrary, by applying the external voltage, the electrons migrated in the opposite direction of the holes. The voltage driven charge carriers mainly tunneled through the nanotubes to its contacted Ti substrate forming photocurrent (Fig. S13), achieving spatial separation of the electron-hole pairs and decreasing their recombination (Fig. 2d).

The PL intensity decreased when the voltage increased from 0 to 1.0 V, and no longer changed when the applied voltage increased further to 1.5 V. Although the increase in the applied voltage can enhance the electric field intensity to induce charge separation further, the rise in the temperature within the catalyst, caused by the higher current through the Ti substrate resulted in the strong electron-phonon interaction. Electrons and phonons are strongly coupled to induce transient elastic lattice distortions, and photogenerated carriers will be rapidly self-trapped by the distorted lattices and then release PL irradiation by recombination processes [37], thus a slight decrease of the PL intensity was observed when the applied voltage increased from 1.0 V to 1.5 V. For the TNTs, a similar trend but with much more slight extent was observed. The time-resolved PL measurements (Fig. 2e and f) of both kinds of catalysts exhibited a similar behavior as well, from which two components named τ_1 (fast) and τ_2 (slow) corresponding to the magnitudes of A_1 and A_2 as listed in Table S5, could be deduced by fitting the double exponential model, as shown in Eq. (2) [38–40]:

$$I(t) = A_1 \exp(-t / \tau_1) + A_2 \exp(-t / \tau_2) \quad (2)$$

where τ_1 was attributed to the radiative emission from the direct recombination of interband excitons, while τ_2 was attributed to the emission from the indirect recombination of the defect-trapped carriers with their counter ones. The direct recombination of excitons was predominant in both the R-TNTs and TNTs, as revealed by the higher proportion of the short-lived component (A_1 , 55.2% for the R-TNTs and 69.3% for the TNTs). The intensity-weighted average lifetime of carriers (τ) prolonged from 4.1 ns to 5.7 ns upon the self-doping. Applying the voltage on the catalyst did not change the dominant recombination of excitons for the TNTs in contrast to that of the R-TNTs. Most impressively, when the voltage was under 0.5, 1.0, and 1.5 V, the τ_2 of the recombination of the defect-trapped carriers increased from 12.6 to 16.8, 28.3 and 28.7 ns, respectively, along with the proportion of the long-lived defect level component which immensely increased to 44.8% and ~85.4% (Table S5). For the TNTs, the τ_2 slightly increased from 13.3 to 14.7 ns, accompanied by a slightly increased proportion of A_2 from 30.8% to 40.0%. Combined with the results obtained from the steady-state PL analysis, it could be inferred that the application of external voltage on R-TNTs greatly quenched the recombination of the mobile electrons with the OVs, and concurrently slowed down the recombination of the free and the trapped charge carriers. In brief, the external voltage inhibited recombination that caused by defects.

3.3. Electric assisted photocatalytic performance

Under the electric-assisted conditions, the recombination of the photogenerated charge carriers can be greatly inhibited, and strong photoexcited electron fluxes can be dragged out of the catalyst to realize spatial separation of the carriers. Cocatalysts can function as active sites for heterogeneous photocatalysts to improve their activity and selectivity. Therefore, TiO_2 nanotube films with Pt, Pd, and Au cocatalysts were used for WSR, ORR, and CO_2 -PR, respectively. For the catalysts with Pt, Pd, and Au deposition, no characteristic peaks were observed in the XRD analyses (Fig. S14) because the high degree of dispersion or the trace quantities of the metals. They were further characterized by high-resolution transmission electron-microscopy (HR-TEM) and high-angle annular dark-field transmission electron microscopy (HAADF-TEM) to identify the metal deposition sites on the R-TNTs. Fig. 3a–c shows the metal deposited catalysts, where the bright spots seen on the R-TNTs are the metallic nanoparticles with sizes between 2 and 12 nm, originated from the strong Z-contrast character [41]. Energy dispersive X-ray spectroscopy (EDS) mapping further confirmed that the deposited metallic nanoparticles distributed throughout the R-TNTs support originated from Pt, Pd, and Au. The results of inductively coupled plasma optical emission spectrometry (ICP-OES) indicated that the mass contents of Pt, Pd and Au were in the range of 0.23–0.27 wt% (Table S6). In addition, the XPS spectra of Pt 4f (Fig. 3d), Pd 3d (Fig. 3e), and Au 4f (Fig. 3f) further confirmed that Pt^0 , Pd^0 and Au^0 species were on the R-TNTs. Therein, the formation of Schottky junction was resulted from the intimate contact of metal (Pt, Pd and Au) with semiconductor (TNTs and R-TNTs). Based on metal–semiconductor contact theory, the contact potential and electric field can be estimated [42]:

$$V_0 = \frac{eN_D}{\epsilon\epsilon_0} \left(\frac{W^2}{2} - \frac{r_M^2}{6} - \frac{W^3}{3r_M} \right) \quad (3)$$

$$F = \frac{eN_D}{3\epsilon\epsilon_0} r_M^2 (W^3 - r_M^3) \quad (4)$$

where $V_0 = (\Phi_{SC} - \Phi_M)/e$, Φ_M is work function of metals, Φ_{SC} is work function of semiconductor (4.44 eV for R-TNTs), e is the electronic charge (1.60×10^{-19} C), N_D is the donor concentration, ϵ is the dielectric constant (for the self-doped TiO_2 , $\epsilon = 10$), ϵ_0 is the permittivity of vacuum (8.85×10^{-12} F m $^{-1}$), W is the depletion length, r_M is the metal radius.

As shown in Table S7, the estimated values of interfacial electric field were in the range of 10^6 – 10^7 V cm $^{-1}$. The applied slight external electric field (0.25–0.75 V cm $^{-1}$) was extremely lower so that it would not affect the charge transfer between the metal and semiconductor interface.

Also, the band gap energy (E_g) of R-TNTs was evaluated to be 3.25 eV by an ultraviolet photoelectron spectrometer (UPS), with a high enough valence band (VB) potential (2.69 V vs. NHE (normal hydrogen electrode) at pH = 0) for oxidizing H_2O into O_2 (1.23 V), and a conduction band (CB) potential (−0.56 V) suitable for reducing O_2 and CO_2 (Fig. S15). Theoretically, the deposition of metals has no effect on the E_g of the catalysts.

Before evaluating the photocatalytic performance enhancement by electric assistance, several blank experiments were performed for the fabricated catalyst composite in advance. This included (i) treating the reactive system composed of the catalyst with 1.0 V under dark conditions and (ii) irradiating the reactive system without a catalyst. No reactive products were found in the aforementioned cases over an extended reaction period of 3 h (Fig. S16), suggesting that the catalyst could not perform the catalysis simply on the application of a voltage.

Using the Au/R-TNTs film, CH_4 and C_2H_6 were produced during CO_2 photoconversion in the gas phase. Applying an external voltage greater than 0 but lower than 1.0 V inhibited the recombination caused by the defects, drove much more photoelectrons out of the doped catalyst, and enhanced the CO_2 photoreduction to yield both CH_4 (Fig. 4a) and C_2H_6

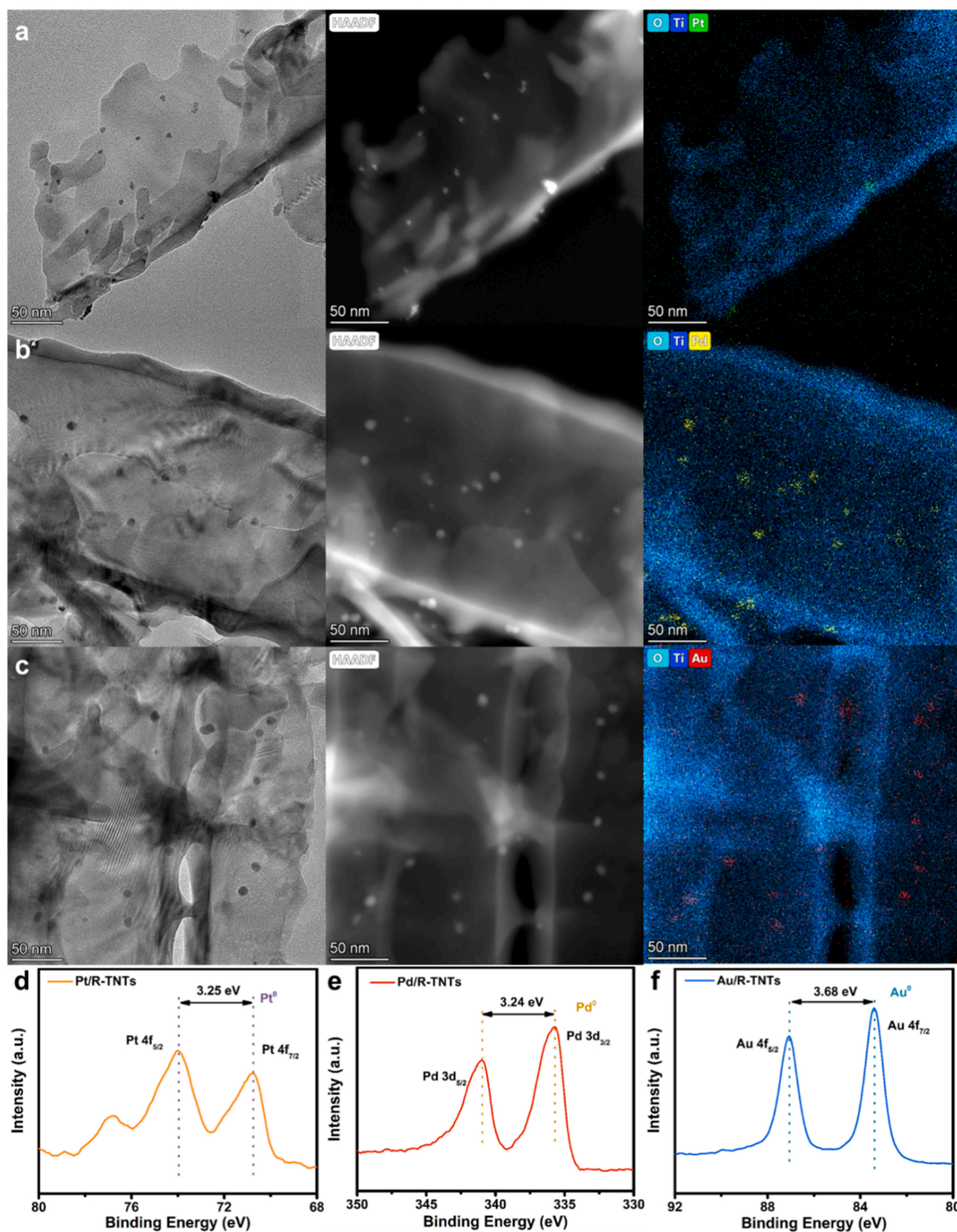


Fig. 3. HR-TEM and HAADF-TEM images of (a) the Pt/R-TNTs, (b) the Pd/R-TNTs, and (c) the Au/R-TNTs. Elemental mappings displayed the distribution of O (cyan), Ti (blue), Pt (green), Pd (yellow), and Au (red). High resolution XPS of (d) the Pt 4f, (e) Pd 3d, and (f) Au 4f spectra for the Pt/R-TNTs, the Pd/R-TNTs, and the Au/R-TNTs catalysts, respectively. (For interpretation of the references to colour in this figure legend, the reader is referred to the web version of this article.).

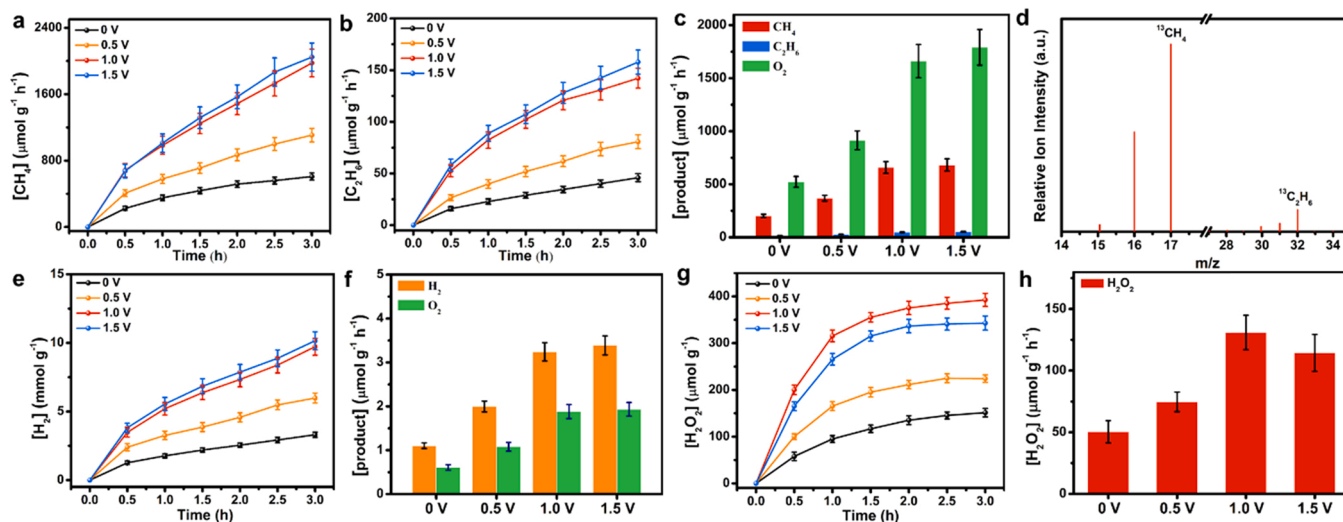


Fig. 4. Cumulative generation of (a) CH₄ and (b) C₂H₆, (c) the generation rates with the Au/R-TNTs under different external voltages. (d) MS signals of a ¹³CO₂ isotope labeling test. Cumulative generation of (e) H₂ and (f) the generation rates with the Pt/R-TNTs under different external voltages. Cumulative generation of (g) H₂O₂ and (h) the generation rates with the Pd/R-TNTs under different external voltages.

(Fig. 4b). Further increase of the voltage beyond 1.0 V (to 1.5 V) changed the yields insignificantly (Table S8), which is consistent with no more changes in the PL intensity over the same voltage range. The maximum rates of CO₂ conversion achieved were 682.3 $\mu\text{mol g}^{-1} \text{h}^{-1}$ and 52.6 $\mu\text{mol g}^{-1} \text{h}^{-1}$ for CH₄ and C₂H₆, respectively, indicating a 3.5-fold enhancement in the photocatalytic performance under electric assistance compared to the photocatalysis (Fig. 4c). A ¹³CO₂ isotope labeling test confirmed the source of reduction products in the process of electric-assisted photocatalysis, in which the signals (Fig. 4d and Fig. S17) of the isotopic ¹³CH₄ and ¹³C₂H₆ appeared at $m/z = 17$ and 32, respectively, and their fragment ions were observed at $m/z = 15$, 16, 30, and 31, respectively [43,44]. Furthermore, the technique is equally suitable for alternative reaction systems using R-TNTs-based photocatalysts, and their photocatalytic performances exhibit similar trends of enhancement with increasing voltage. For example, on applying the voltage of 1.0 or 1.5 V on the Pt/R-TNTs (Table S9) and the Pd/R-TNTs (Table S10) films, the generation of H₂ from the photolysis of distilled water (Fig. 4e and f), and H₂O₂ from O₂ reduction reaction (Fig. 4g and h) increased to about 3 fold, achieving the highest generation rates of H₂ and H₂O₂, up to 3387.5 $\mu\text{mol g}^{-1} \text{h}^{-1}$ and 130.8 $\mu\text{mol g}^{-1} \text{h}^{-1}$, respectively. Inverting the voltage polarity at the two ends of the catalyst film had no impact on its photocatalytic efficiency or the products formed.

Due to the higher current through the Ti substrate, the temperature gradually rose during the electro-assisted photocatalysis process, and asymptotically approached almost a constant temperature after 0.5 h (Fig. S18). Although the rise in temperature promoted the reaction rate to a certain extent, strong electron-phonon interaction would induce self-trapping of the photogenerated carriers, accelerating their recombination rate. In these systems, it is obvious that the recombination of photogenerated carriers by the temperature played a dominant role in the photocatalytic performance, which led to the lower net reaction rate in the subsequent reaction period than that in the first 0.5 h.

As for the decrease in the H₂O₂ production with the increase of voltage up to 1.5 V, it may be attributed to the accelerated decomposition of H₂O₂ during the reaction, considering the similar amount of products should be produced under both the 1.0 V and 1.5 V. Although the external voltage caused the rise in temperature within the system, blank experiments performed at 37 and 45 °C corresponding to 1.0 and 1.5 V, respectively, excluded the possibility of photothermal decomposition of H₂O₂ (Fig. S19). On the other hand, it is well-documented that the surface groups of Ti-OH on the TiO₂ can catalytically decompose the generated H₂O₂ via photogenerated electrons (Eqs. 5 and 6) [45]. It is

obvious that the voltage of 1.5 V accelerated the decompose reaction (Fig. S19), resulting in a drop in the net production rate of H₂O₂.



In addition, it is worth noting that all the R-TNTs-based photocatalysts showed better photocatalytic performance than that of their counterpart TNTs-based photocatalysts (Tables S8–S10). Owing to the high conductivity and carrier concentration, compared with the TNTs-based photocatalysts, a larger population of photogenerated carriers in the R-TNTs-based catalyst would react with reactant molecules under the same illumination conditions. Furthermore, applying external voltages to the undoped films of the Pt/TNTs, Pd/TNTs, and Au/TNTs, had an insignificant impact on their photocatalytic performance (Fig. S20). Due to their lower carrier mobility, it is difficult to separate much more photogenerated carriers from the bulk of TNTs-based photocatalysts with the slight external voltage. They would be rapidly recombined, accompanied with PL irradiation. Moreover, the R-TNTs-based photocatalysts have advantages over other representative photocatalysts that higher photocatalytic activity can be obtained, especially under the electric assistance (Table S11) without requirements for sacrificial agents in the WSR, ORR, and CO₂-PR.

In the aforementioned photocatalytic reactions, a half-reaction comprising water oxidation on the VB of the semiconductor is essential for the development of a viable technology for chemical conversion [46–48]. The oxidation not only provides the protons for the hydrogenation, but also evolves O₂ as a by-product (OER). The maximum generation rate of O₂ was found to be 1932.2 $\mu\text{mol g}^{-1} \text{h}^{-1}$ and 1791.1 $\mu\text{mol g}^{-1} \text{h}^{-1}$ in the WSR and the CO₂-PR, respectively. The ratio of the consumed number of electrons to holes for the photocatalytic redox in the two systems was approximately 1:1.10–1:1.16, indicating that their participation in the photoreaction was almost comparable. Moreover, the catalytic performance remained fairly stable and active for at least four cycles of the repetition test (Fig. S21). After the reaction, no obvious changes were observed in the lattice orientation (Fig. S22), the valence states of the metals (Fig. S23), the particle size (Fig. S24) and the mass contents (Table S6) of metals compared with the original sample.

From the operando TRPL measurements under CO₂ and Ar atmospheres (Fig. S25), the rate of electron transfer from the trapped states to the adsorbed CO₂ can be estimated. The rate was roughly estimated to be

$4.3 \times 10^6 \text{ s}^{-1}$ with both 0 and 1.5 V, as calculated by $(\text{CO}_2\text{-}\tau)^{-1} - (\text{Ar-}\tau)^{-1}$, where $\text{CO}_2\text{-}\tau$ and $\text{Ar-}\tau$ are the average lifetimes of the PL spectra for the Au/R-TNTs under CO_2 and Ar atmospheres (Table S12) [49]. Assuming that the excitation of the catalysts was of equal probability under the same light source, exerting the voltage on the catalysts did not change the interfacial electron transfer from the excited photocatalyst film to the adsorbed CO_2 .

Because a major fraction of the photoexcited electrons is freely distributed within the bulk of the catalysts and rapidly recombines at room temperature, dragging them out by the external voltage generates a large photocurrent, which greatly improves the photocatalytic performance of the metal-deposited R-TNTs catalyst. In general, defects, especially in the bulk of the photocatalyst, function as recombination centers. The voltage applied to the catalyst suppressed the recombination of defects. Specifically, driven by the external voltage, the barriers to the photogenerated electrons and holes migrating in opposite directions in the high conductive semiconductor became lower, which led to the efficient spatial separation of the charge carriers, thereby increasing the efficiency of the heterogeneous reactions. The photocatalytic performance in response to external voltages is in complete agreement with the quenching behavior of the PL signals.

4. Conclusions

In summary, a sufficiently striking and advanced electric-assisted photocatalytic system was developed for the use in both liquid- and gas-phase reactions such as water splitting, H_2O_2 synthesis, and CO_2 photoreduction. Applying a slight voltage to a self-doped TNTs-based photocatalyst film can significantly improve its photocatalytic efficiency. A comprehensive analysis of the results associated with the transient photocurrent, electronic properties, operando steady-state photoluminescence, and time resolved photoluminescence analysis, demonstrated that the self-doping treatment generated a high concentration of carriers in the TNTs, resulting in a significant promotion of conductivity and carrier mobility. Under the electric assistance, recombination of the photogenerated charge carriers is greatly suppressed, and the photoexcited electrons are expelled from the catalyst to realize spatial separation of the carriers. The photocatalytic redox reactions are integrated on one sheet of the film in the electric-assisted system, as opposed to the conventional PEC that occurs on a separated electrode. Owing to its effectiveness and utility, the electric-assisted photocatalytic technique has great potential to transverse the gap between laboratory experiments and industrial-scale applications, in both liquid and gas phases.

CRedit authorship contribution statement

Honghui Pan: Data curation, Investigation, Writing – original draft. **Minghui Sun:** Formal analysis, Validation, Methodology. **Xiaoguang Wang:** Data curation, Formal analysis. **Ming Zhang:** Writing – review & editing. **Muthu Murugananthan:** Writing – review & editing. **Yanrong Zhang:** Funding acquisition, Project administration, Conceptualization, Resources, Writing – review & editing.

Declaration of Competing Interest

The authors declare that they have no known competing financial interests or personal relationships that could have appeared to influence the work reported in this paper.

Acknowledgments

This work was partially supported by the National Key Research and Development Program of China (No. 2020YFC1908704), International Science & Technology Cooperation Program of China (No. 2016YFE0126300), the National Natural Science Foundation of China

(52070082). The authors thank the Analytical and Testing Center of HUST for the use of SEM, TEM, PL and TRPL equipment.

Appendix A. Supporting information

Supplementary data associated with this article can be found in the online version at doi:10.1016/j.apcatb.2022.121174.

References

- [1] A. Meng, L. Zhang, B. Cheng, J. Yu, Dual cocatalysts in TiO_2 photocatalysis, *Adv. Mater.* 31 (2019), 1807660, <https://doi.org/10.1002/adma.201807660>.
- [2] X. Li, J. Yu, M. Jaroniec, X. Chen, Cocatalysts for selective photoreduction of CO_2 into solar fuels, *Chem. Rev.* 119 (2019) 3962–4179, <https://doi.org/10.1021/acs.chemrev.8b00400>.
- [3] S. Cao, J. Low, J. Yu, M. Jaroniec, Polymeric photocatalysts based on graphitic carbon nitride, *Adv. Mater.* 27 (2015) 2150–2176, <https://doi.org/10.1002/adma.201500033>.
- [4] T. Banerjee, F. Podjaski, J. Kröger, B.P. Biswal, B.V. Lotsch, Polymer photocatalysts for solar-to-chemical energy conversion, *Nat. Rev. Mater.* 6 (2020) 168–190, <https://doi.org/10.1038/s41578-020-00254-z>.
- [5] D. Li, M. Kassymova, X. Cai, S.-Q. Zang, H.-L. Jiang, Photocatalytic CO_2 reduction over metal-organic framework-based materials, *Coord. Chem. Rev.* 412 (2020), 213262, <https://doi.org/10.1016/j.ccr.2020.213262>.
- [6] J. Qiu, X. Zhang, Y. Feng, X. Zhang, H. Wang, J. Yao, Modified metal-organic frameworks as photocatalysts, *Appl. Catal. B* 231 (2018) 317–342, <https://doi.org/10.1016/j.apcatb.2018.03.039>.
- [7] Q. Yang, M. Luo, K. Liu, H. Cao, H. Yan, Covalent organic frameworks for photocatalytic applications, *Appl. Catal. B* 276 (2020), 119174, <https://doi.org/10.1016/j.apcatb.2020.119174>.
- [8] R.K. Sharma, P. Yadav, M. Yadav, R. Gupta, P. Rana, A. Srivastava, R. Zboril, R. S. Varma, M. Antonietti, M.B. Gawande, Recent development of covalent organic frameworks (COFs): synthesis and catalytic (organic-electro-photo) applications, *Mater. Horiz.* 7 (2020) 411–454, <https://doi.org/10.1039/C9MH00856J>.
- [9] S. Bai, N. Zhang, C. Gao, Y. Xiong, Defect engineering in photocatalytic materials, *Nano Energy* 53 (2018) 296–336, <https://doi.org/10.1016/j.nanoen.2018.08.058>.
- [10] Z. Zafar, S.S. Yi, J.P. Li, C.Q. Li, Y.F. Zhu, A. Zada, W.J. Yao, Z.Y. Liu, X.Z. Yue, Recent development in defects engineered photocatalysts: an overview of the experimental and theoretical strategies, *Energy Environ. Mater.* 0 (2021) 1–47, <https://doi.org/10.1002/eem2.12171>.
- [11] Z. Xiu, M. Guo, T. Zhao, K. Pan, Z. Xing, Z. Li, W. Zhou, Recent advances in Ti^{3+} self-doped nanostructured TiO_2 visible light photocatalysts for environmental and energy applications, *Chem. Eng. J.* 382 (2020), 123011, <https://doi.org/10.1016/j.cej.2019.123011>.
- [12] R. Hahn, F. Schmidt-Stein, J. Salonen, S. Thiemann, Y. Song, J. Kunze, V.-P. Lehto, P. Schmuki, Semimetallic TiO_2 nanotubes, *Angew. Chem. Int. Ed.* 48 (2009) 7236–7239, <https://doi.org/10.1002/anie.200902207>.
- [13] J. Li, M. Zhang, Z. Guan, Q. Li, C. He, J. Yang, Synergistic effect of surface and bulk single-electron-trapped oxygen vacancy of TiO_2 in the photocatalytic reduction of CO_2 , *Appl. Catal. B* 206 (2017) 300–307, <https://doi.org/10.1016/j.apcatb.2017.01.025>.
- [14] C. Mao, H. Cheng, H. Tian, H. Li, W.-J. Xiao, H. Xu, J. Zhao, L. Zhang, Visible light driven selective oxidation of amines to imines with BiOCl : does oxygen vacancy concentration matter? *Appl. Catal. B* 228 (2018) 87–96, <https://doi.org/10.1016/j.apcatb.2018.01.018>.
- [15] H. Wu, H.L. Tan, C.Y. Toe, J. Scott, L. Wang, R. Amal, Y.H. Ng, Photocatalytic and photoelectrochemical systems: similarities and differences, *Adv. Mater.* 32 (2019), 1904717, <https://doi.org/10.1002/adma.201904717>.
- [16] D. Monllor-Satoca, M.I. Díez-García, T. Lana-Villarreal, R. Gómez, Photoelectrocatalytic production of solar fuels with semiconductor oxides: materials, activity and modeling, *Chem. Commun.* 56 (2020) 12272–12289, <https://doi.org/10.1039/D0CC04387G>.
- [17] B. Gao, M. Sun, W. Ding, Z. Ding, W. Liu, Decoration of γ -graphyne on TiO_2 nanotube arrays: improved photoelectrochemical and photoelectrocatalytic properties, *Appl. Catal. B* 281 (2021), 119492, <https://doi.org/10.1016/j.apcatb.2020.119492>.
- [18] L. Li, S. Xiao, R. Li, Y. Cao, Y. Chen, Z. Li, G. Li, H. Li, Nanotube array-like WO_3 photoanode with dual-layer oxygen-evolution cocatalysts for photoelectrocatalytic overall water splitting, *ACS Appl. Energy Mater.* 1 (2018) 6871–6880, <https://doi.org/10.1021/acsami.8b01215>.
- [19] G. Li, Z. Lian, W. Wang, D. Zhang, H. Li, Nanotube-confinement induced size-controllable g-C $_3$ N $_4$ quantum dots modified single-crystalline TiO_2 nanotube arrays for stable synergistic photoelectrocatalysis, *Nano Energy* 19 (2016) 446–454, <https://doi.org/10.1016/j.nanoen.2015.10.011>.
- [20] D. Jesić, D. Lasić Jurković, A. Pohar, L. Suhadolnik, B. Likozar, Engineering photocatalytic and photoelectrocatalytic CO_2 reduction reactions: mechanisms, intrinsic kinetics, mass transfer resistances, reactors and multi-scale modelling simulations, *Chem. Eng. J.* 407 (2021), 126799, <https://doi.org/10.1016/j.cej.2020.126799>.
- [21] S. Xie, Q. Zhang, G. Liu, Y. Wang, Photocatalytic and photoelectrocatalytic reduction of CO_2 using heterogeneous catalysts with controlled nanostructures, *Chem. Commun.* 52 (2016) 35–59, <https://doi.org/10.1039/C5CC07613G>.

- [22] B. Shan, S. Vanka, T.-T. Li, L. Troian-Gautier, M.K. Brennaman, Z. Mi, T.J. Meyer, Binary molecular-semiconductor p-n junctions for photoelectrocatalytic CO₂ reduction, *Nat. Energy* 4 (2019) 290–299, <https://doi.org/10.1038/s41560-019-0345-y>.
- [23] Y. Dou, A. Zhou, Y. Yao, S.Y. Lim, J.-R. Li, W. Zhang, Suppressing hydrogen evolution for high selective CO₂ reduction through surface-reconstructed heterojunction photocatalyst, *Appl. Catal. B* 286 (2021), 119876, <https://doi.org/10.1016/j.apcatb.2021.119876>.
- [24] R.M. Sellers, Spectrophotometric determination of hydrogen peroxide using potassium titanium(IV) oxalate, *Analysis* 105 (1980) 950–954, <https://doi.org/10.1039/AN9800500950>.
- [25] X. Wang, M. Sun, M. Murugananthan, Y. Zhang, L. Zhang, Electrochemically self-doped WO₃/TiO₂ nanotubes for photocatalytic degradation of volatile organic compounds, *Appl. Catal. B* 260 (2020), 118205, <https://doi.org/10.1016/j.apcatb.2019.118205>.
- [26] M. Sun, X. Wang, Z. Chen, M. Murugananthan, Y. Chen, Y. Zhang, Stabilized oxygen vacancies over heterojunction for highly efficient and exceptionally durable VOCs photocatalytic degradation, *Appl. Catal. B* 273 (2020), 119061, <https://doi.org/10.1016/j.apcatb.2020.119061>.
- [27] Y. Chen, H.T. Yi, X. Wu, R. Haroldson, Y.N. Gartstein, Y.I. Rodionov, K. S. Tikhonov, A. Zakhidov, X.Y. Zhu, V. Podzorov, Extended carrier lifetimes and diffusion in hybrid perovskites revealed by hall effect and photoconductivity measurements, *Nat. Commun.* 7 (2016) 12253, <https://doi.org/10.1038/ncomms12253>.
- [28] H. Zhou, Y. Zhang, Electrochemically self-doped TiO₂ nanotube arrays for supercapacitors, *J. Phys. Chem. C* 118 (2014) 5626–5636, <https://doi.org/10.1021/jp4082883>.
- [29] F. Fabregat-Santiago, G. Garcia-Belmonte, J. Bisquert, P. Bogdanoff, A. Zaban, Mott-schottky analysis of nanoporous semiconductor electrodes in dielectric state deposited on SnO₂(F) conducting substrates, *J. Electrochem. Soc.* 150 (2003) E293–E298, <https://doi.org/10.1149/1.1568741>.
- [30] C. Wehrenfennig, C.M. Palumbini, H.J. Snaith, M.B. Johnston, L. Schmidt-Mende, L.M. Herz, Fast charge-carrier trapping in TiO₂ nanotubes, *J. Phys. Chem. C* 119 (2015) 9159–9168, <https://doi.org/10.1021/acs.jpcc.5b01827>.
- [31] R. Li, F. Zhang, D. Wang, J. Yang, M. Li, J. Zhu, X. Zhou, H. Han, C. Li, Spatial separation of photogenerated electrons and holes among {010} and {110} crystal facets of BiVO₄, *Nat. Commun.* 4 (2013) 1432, <https://doi.org/10.1038/ncomms2401>.
- [32] D.K. Pallotti, L. Passoni, P. Maddalena, F. Di Fonzo, S. Lettieri, Photoluminescence mechanisms in anatase and rutile TiO₂, *J. Phys. Chem. C* 121 (2017) 9011–9021, <https://doi.org/10.1021/acs.jpcc.7b00321>.
- [33] C.C. Mercado, F.J. Knorr, J.L. McHale, Observation of charge transport in single titanium dioxide nanotubes by micro-photoluminescence imaging and spectroscopy, *ACS Nano* 6 (2012) 7270–7280, <https://doi.org/10.1021/nn302392p>.
- [34] X. Zhang, Q. Liao, S. Liu, Z. Kang, Z. Zhang, J. Du, F. Li, S. Zhang, J. Xiao, B. Liu, Y. Ou, X. Liu, L. Gu, Y. Zhang, Poly(4-styrenesulfonate)-induced sulfur vacancy self-healing strategy for monolayer MoS₂ homojunction photodiode, *Nat. Commun.* 8 (2017) 15881, <https://doi.org/10.1038/ncomms15881>.
- [35] E. Silva Junior, F.A. La Porta, M.S. Liu, J. Andrés, J.A. Varela, E. Longo, A relationship between structural and electronic order–disorder effects and optical properties in crystalline TiO₂ nanomaterials, *Dalton Trans.* 44 (2015) 3159–3175, <https://doi.org/10.1039/C4DT03254C>.
- [36] Z. Zhang, J.T. Yates, Band bending in semiconductors: chemical and physical consequences at surfaces and interfaces, *Chem. Rev.* 112 (2012) 5520–5551, <https://doi.org/10.1021/cr3000626>.
- [37] L. Zhou, J.F. Liao, Z.G. Huang, J.H. Wei, X.D. Wang, H.Y. Chen, D.B. Kuang, Intrinsic self-trapped emission in 0D lead-free (C₆H₁₄N₂)₂In₂Br₁₀ single crystal, *Angew. Chem. Int. Ed.* 58 (2019) 15435–15440, <https://doi.org/10.1002/anie.201907503>.
- [38] M.V. Dozzi, C. D'Andrea, B. Ohtani, G. Valentini, E. Selli, Fluorine-doped TiO₂ materials: photocatalytic activity vs time-resolved photoluminescence, *J. Phys. Chem. C* 117 (2013) 25586–25595, <https://doi.org/10.1021/jp4095563>.
- [39] K. Iijima, M. Goto, S. Enomoto, H. Kunugita, K. Ema, M. Tsukamoto, N. Ichikawa, H. Sakama, Influence of oxygen vacancies on optical properties of anatase TiO₂ thin films, *J. Lumin.* 128 (2008) 911–913, <https://doi.org/10.1016/j.jlumin.2007.11.071>.
- [40] H. Li, H. Shang, Y. Li, X. Cao, Z. Yang, Z. Ai, L. Zhang, Interfacial charging–discharging strategy for efficient and selective aerobic NO oxidation on oxygen vacancy, *Environ. Sci. Technol.* 53 (2019) 6964–6971, <https://doi.org/10.1021/acs.est.9b01287>.
- [41] Q. Wang, X. Huang, Z.L. Zhao, M. Wang, B. Xiang, J. Li, Z. Feng, H. Xu, M. Gu, Ultrahigh-loading of Ir single atoms on NiO matrix to dramatically enhance oxygen evolution reaction, *J. Am. Chem. Soc.* 142 (2020) 7425–7433, <https://doi.org/10.1021/jacs.9b12642>.
- [42] T. Ioannides, X.E. Verykios, Charge transfer in metal catalysts supported on doped TiO₂: a theoretical approach based on metal–semiconductor contact theory, *J. Catal.* 161 (1996) 560–569, <https://doi.org/10.1006/jcat.1996.0218>.
- [43] Y. Liu, C. Miao, P. Yang, Y. He, J. Feng, D. Li, Synergetic promotional effect of oxygen vacancy-rich ultrathin TiO₂ and photochemical induced highly dispersed Pt for photoreduction of CO₂ with H₂O, *Appl. Catal. B* 244 (2019) 919–930, <https://doi.org/10.1016/j.apcatb.2018.12.028>.
- [44] S. Sorcar, J. Thompson, Y. Hwang, Y.H. Park, T. Majima, C.A. Grimes, J.R. Durrant, S.-I. In, High-rate solar-light photoconversion of CO₂ to fuel: controllable transformation from C₁ to C₂ products, *Energy Environ. Sci.* 11 (2018) 3183–3193, <https://doi.org/10.1039/C8EE00983J>.
- [45] H. Hou, X. Zeng, X. Zhang, Production of hydrogen peroxide by photocatalytic processes, *Angew. Chem. Int. Ed.* 59 (40) (2020) 17356–17376, <https://doi.org/10.1002/anie.v59.4010.1002/anie.201911609>.
- [46] Y. Wang, X. Shang, J. Shen, Z. Zhang, D. Wang, J. Lin, J.C.S. Wu, X. Fu, X. Wang, C. Li, Direct and indirect Z-scheme heterostructure-coupled photosystem enabling cooperation of CO₂ reduction and H₂O oxidation, *Nat. Commun.* 11 (2020) 3043, <https://doi.org/10.1038/s41467-020-16742-3>.
- [47] J.K. Hurst, In pursuit of water oxidation catalysts for solar fuel production, *Science* 328 (2010) 315–316, <https://doi.org/10.1126/science.1187721>.
- [48] F. He, B. Zhu, B. Cheng, J. Yu, W. Ho, W. Macyk, 2D/2D/0D TiO₂/C₃N₄/Ti₃C₂ MXene composite S-scheme photocatalyst with enhanced CO₂ reduction activity, *Appl. Catal. B Environ.* 272 (2020), 119006, <https://doi.org/10.1016/j.apcatb.2020.119006>.
- [49] H. Li, J. Shang, Z. Ai, L. Zhang, Efficient visible light nitrogen fixation with BiOBr nanosheets of oxygen vacancies on the exposed {001} facets, *J. Am. Chem. Soc.* 137 (2015) 6393–6399, <https://doi.org/10.1021/jacs.5b03105>.